The cancer-specific lncRNA *LISR* customizes ribosomes to suppress anti-tumour immunity

Sonia Cinque[1], Yvessa Verheyden[1,], Vicky Katopodi[1,*], Zorica Knezevic[1], Ewout Demesmaeker[1], Sara Adnane[1], Sarah Hanache[1], Roberto Vendramin[1], Fabian Stinkens[1,2], Felicia Vervloesem[1,2] Alessandro Cuomo[3], Joanna Pozniak[4], Alvaro Cortes Calabuig[5],* Sébastien Tabruyn[6], *Oliver Bechter[7,§], Maria Francesca Baietti[1,2,§], Elisabetta Groaz[8,9,§], Tiziana Bonaldi[3,10], Eleonora Leucci[1,2,#]*

[1]Laboratory for RNA Cancer Biology, Department of Oncology, KU Leuven, Leuven, Belgium. [2]Trace, Leuven Cancer Institute, KULeuven, Leuven, Belgium Department of Experimental Oncology, IEO, European Institute of Oncology IRCCS, Via Adamello 16, 20139 Milan, Italy. [4]Laboratory for Molecular Cancer Biology, Center for Cancer Biology, VIB, Leuven, Belgium. [5]Laboratory for Cytogenetics and Genome Research, Department of Human Genetics, KULeuven, Leuven, Belgium. [6]TransCure bioServices, Archamps France. [7]Department of General Medical Oncology UZ Leuven, Leuven, Belgium [8]Rega Institute for Medical Research, Medicinal Chemistry, KU Leuven, Leuven, Belgium. [9]Department of Pharmaceutical and Pharmacological Sciences, University of Padova, Padova, Italy.[10]Department of Oncology and Hematology-Oncology, University of Milan, Milan, 20122 Italy.

* and § indicate equal contribution

#Corresponding Author
Dr Eleonora Leucci,
Laboratory for RNA Cancer Biology
Department of Oncology, LKI, KU Leuven
Campus Gasthuisberg, Onderwijs en Navorsing 4
Herestraat 49, bus 818
3001 LEUVEN
E-mail: eleonora.leucci@kuleuven.be
Phone: +32 16 32 32 16

Abstract

Responses to anticancer therapies in patients with advanced metastatic disease are often lower than 50% and the majority of patients initially responding develop resistance later on. Therapy resistance often follows an adaptation phase in which cancer cells exit the cell cycle and engage the Integrated Stress Response (ISR). Activation of this pathway induces the emergence of drug-tolerant persister cells via the block of CAP-dependent translation while enhancing translation of select mRNAs that support survival, migration and dampen immunogenicity. Little is known about the molecular mechanisms underlying ISR-dependent immune escape. Searching for transcripts specifically associated with polysomes upon ISR activation we identified the lncRNA *LISR.* We showed that this untranslated transcript, could suppress the production of putative neoantigens, while promoting translation of *PD-L1* and other mRNAs involved in the formation of the glycocalyx. Accordingly, *LISR* locus is amplified in 60% of melanomas and its expression is increased in patients refractory to Immune Checkpoint Blockade (ICB). Consequently, inhibition of *LISR* stimulated anti-tumour immune responses both *in vitro* and in humanized and ICB-resistant patient-derived xenografts. This study establishes a link between lncRNAs, translation rewiring in cancer and immunogenicity, and identifies an RNA-based cancer-specific therapeutic strategy to overcome intrinsic resistance to ICB.

Introduction

Although the response rate to anticancer targeted therapies may be relatively high in some specific contexts, such as BRAF-mutant melanoma for instance, the benefits of such treatments are limited by the development of secondary resistance. This is because, even if combined, agents that target dysregulated oncogenic pathways do not eradicate all cells, leaving behind a pool of drug-tolerant persister cells from which resistance will invariably develop. DTPCs may pre-exist and, thereby, be positively selected by the therapy and/or emerge from a pool of cells that acquire a drug-tolerant phenotype through non-genetic reprogramming [1].

One of the key non-genetic mechanisms leading to the generation of DTPCs is driven by a cytoplasmic adaptive response to intracellular and extracellular stress stimuli (e.g., amino acids deprivation, inflammation, ER stress…), known as the Integrated Stress Response (ISR). This pathway causes a global reduction of CAP-dependent translation initiation and activation of special transcriptional and translational programs orchestrated by the transcription factor ATF4. By coordinating the unfolded protein response, amino acid metabolism and oxidative stress responses, among the others [2, 3], ATF4 promotes DCPCs survival.

The selective recruitment to ribosomes and translation of specific pro-survival mRNAs that promote the survival of DTPCs, is believed to rely mostly on structural motifs (e.g., G-quadruplexes, IRES…) on the mRNAs. Whether trans-acting factors are also involved in this recruitment process is yet unknown but is a likely and interesting possibility. While canonical coding and non-coding components of the translational machinery (e.g., ribosomal proteins, tRNAs, rRNAs) and their transcriptional, post-transcriptional and post-translational modifications [4] are emerging as critical regulators of translational rewiring in cancer. Whether long non-coding RNAs

(lncRNAs), a large fraction of which is associated with ribosomes [5-8], also contribute to translation adaptation remains underexplored. It has been proposed that lncRNA binding to ribosomes may modulate their biogenesis and/or the recruitment/translation of selected mRNAs [9-11]. Moreover an handful of these transcripts (~2-7%) seems to produce (micro)peptides [12-15], some of which with a reported function [16-18]. The possibility that lncRNAs participate to the generation of a cancer-specific ribosome and/or translatome landscape [19, 20] during cancer cell adaptation to therapy, and thereby to the emergence of DTPCs, has not yet been examined.

The ISR has emerged as a key regulator of resistance to targeted therapy in several cancers [21]. In melanoma, the ISR tunes down expression of the key transcription factor MITF and, thereby, promotes de-differentiation and a progressive transition to a mesenchymal-like/invasive cell state [22]. This phenotype switch is accompanied by a decrease in cell proliferation, a metabolic rewiring from glycolysis to OXPHOS and increased resistance to MAPK inhibitors [23].

The development of novel classes of immunotherapies, such as immune checkpoint blockade (ICB), has demonstrated remarkable clinical benefits, leading to complete remission in a variety of cancers. However, there are still too many patients that do not exhibit durable survival benefit. How the ISR pathway contributes to resistance to immunotherapy remains unclear.

Recent studies have linked inhibition of CAP-dependent translation to the increase in translation of PD-L1 in liver cancer [24], in melanoma [25] and in human lung cancer cells [26]. Additionally, the increase in IDO1 induced by the ISR converts tryptophan to kynurenine, a metabolite with known immunosuppressive function [27]. These recent data indicate that the activation of the ISR pathway may indeed promote immune escape. However, it has also been reported that, activation of this pathway

by the IFN-γ, may instead increase cancer cell immunogenicity. Notably, interferon signalling is required for the expression of MHC I [27] and increases the repertoire of putative neoantigens by inducing ribosome stalling and frameshifting [28]. Together these apparently conflicting studies have highlighted the need to better understand the role of ISR in anti-tumour immunity and how to manipulate this pathway to overcome therapy resistance.

Here we demonstrated that the immune suppressive and immune stimulatory functions of the ISR can be uncoupled by inhibiting a single cancer-specific lncRNA. Pharmacological inhibition of this lncRNA, named *LISR*, increases melanoma cell immunogenicity and sensitivity to ICB.

Results

LISR is associated with polysomes upon induction of the ISR

To gain insights into the common principles governing translational regulation in therapy resistant melanoma, we performed ribosome profiling and RNA sequencing of 3 Patient-Derived Xenograft (PDX) melanoma models, all derived from patients that developed resistance to MAPKi and/or ICB and shown to have engaged the ISR pathway [23]. By comparing the mRNAs and lncRNAs contents in the different ribosomal fractions (Figure 1A-B), we observed that protein-coding RNAs were equally distributed between the ribosomal subunit and polysome fractions (Figure 1A). In contrast, and consistent with their low coding potential, lncRNAs were instead strongly enriched in the small ribosomal subunit (40S) fraction (Figure 1B). This association with the 40S is suggestive of a putative role of lncRNAs in the regulation of translation initiation.

To identify transcripts that are selectively recruited to polysomes during the establishment of drug-tolerance, we treated SK-MEL-28 melanoma cells with salubrinal, a compound that induces the ISR by inhibiting EIF2α dephosphorylation [22, 24, 25], and performed polysome profiling and RNA-sequencing (Figure 1C). Among the candidates significantly associated with the polysomes, we identified *ENST00000648050.1*, an annotated lncRNA (Supplementary figure 1A), which we renamed *LISR* (for LncRNA ISR Regulator). While mainly associated with the 40S in control samples, *LISR* was strongly enriched to polysomes following ISR activation (Figure 1D). Likewise, *LISR* was also enriched at polysomes in tumours from the above-described therapy-resistant PDX melanoma models (Figure 1E).

Such a shift was unexpected given the low coding potential of *LISR* predicted by the Coding Potential Calculator (CPC2) algorithm (Figure 1F). To rule out the possibility that LISR is translated we therefore performed a thorough proteomic analysis of small and large peptides in control and salubrinal-treated melanoma cells, which failed to detect any peptide arising from *LISR* (Supplementary Table 1). Conversely, peptides derived from two lncRNAs in control samples, but not in salubrinal-treated cells were detected. This analysis confirmed that the majority of lncRNAs, including *LISR*, are not translated in these melanoma cells, and provided evidence that the translation of a small minority of lncRNAs with coding potential is actually repressed upon ISR activation (Figure 1G-H). Importantly, the enrichment of *LISR* at the polysomes could not be explained by an overall increase expression of this transcript, as its levels were largely unchanged in cells treated with salubrinal (see input, Figure 1D). Consistently, depletion of ATF4 in salubrinal-treated cells did not impact *LISR* expression (Supplementary Figure 1D).

LISR, which is a polyadenylated transcript (Supplementary Figure 1C), primarily localiz to the cytoplasm in melanoma cells, as shown by subcellular fractionation (Supplementary Figure 1D) and confirmed by smFISH (Supplementary Figure 1E). Importantly, its cellular distribution remained unchanged upon the ISR induction (Supplementary Figure 1D).

LISR expression correlates with resistance to immunotherapy

Analysis of expression in normal tissues from the Genotype Tissue Expression (GTEX) indicated that *LISR* is mostly undetectable in normal adult tissues (Figure 2A). In contrast, *LISR* expression (Figure 2B) and DNA copy number (Figure 2C) in cancer significantly anticorrelated with patients' survival in the Pan Cancer Atlas (PanCanAtlas) [29]. Consistently, LISR expression was significantly higher in metastatic samples compared to primary tumours (Figure 2D).

The *LISR* locus resides in a region of chromosome 12 (12p11.21) that is amplified in over 60% of melanoma cases (TCGA; Figure 2E). Importantly, the presence of this amplicon was found to be associated with a significantly worse prognosis for melanoma patients (Figure 2F). Additionally, *LISR* expression significantly correlated with the invasive signature associated with targeted therapy resistance in melanoma TCGA dataset [30] (Figure 2G). *LISR* expression could be detected in most short-term and established melanoma lines analysed, irrespective of the driver mutation (Supplementary Figure 1F) and in the majority (7 out of 10) of tumours from PDX melanoma models tested (Supplementary Figure 1G). Notably, the highest expression levels were detected in MEL-058 and MEL-083, two models derived from patients that progressed under targeted and immune therapy, respectively.

In keeping with this, treating a BRAF-mutant PDX model with the MAPK-inhibitors Dabrafenib and Trametinib (DT) promoted emergence of the DTPC population harbouring a mesenchymal-like phenotype [31] and a concomitant increase in *LISR* expression (Figure 2H). However, no significant correlation between *LISR* expression and responses to MAPKi could be detected in a large panel of BRAF mutant lines from the CCLE database (Supplementary Figure 2A-B). Instead, a significant negative correlation was found between *LISR* expression and therapy responses to α-PD-1 in PDX melanoma models (Supplementary Figure 2C-D) and in patients from two independent cohorts [32, 33] (Figure 2I-J). Importantly, in the second cohort, in which data before (BT) and early on-treatment (OT) are available, *LISR* expression was found to be induced by ICB and increased in patients refractory to the therapy [32] (Figure 2J).

These data demonstrate that *LISR* is a cancer-specific lncRNA whose expression and copy number in melanoma, negatively correlate with cancer patients' overall survival and with response to ICB.

Inhibition of *LISR* enhances antimelanoma immune responses *in vitro*

The negative correlation between *LISR* expression and response to ICB prompted us to test whether *LISR* targeting may increase anti-melanoma immune response. We co-cultured IL-2-stimuated PBMCs with HLA matched melanoma cells (MM099) harbouring a mesenchymal-like phenotype, exhibiting pre-existing activation of the ISR and high expression of *LISR* [23] (Supplementary Figure 1F). These co-cultures were either exposed to a non-targeting control Antisense Oligonucleotide (Ctrl ASO) or an ASO targeting *LISR* (Figure 3A-B). As expected, untreated and non-targeting control-transfected mesenchymal-like melanoma cells were poorly immunogenic

[32]. Interestingly, inhibition of *LISR* led to an early increase in the PBMCs proliferation (Supplementary Figure 3A) and a significant induction of melanoma cell killing (Figure 3C-D), as demonstrated by the decrease in melanoma cell confluency (Figure 3C) and increase in Caspase-3-positive cell counts (Figure 3D). To test whether T-cells are responsible for melanoma cell killing, we activated the PBMCs with a T-cell cocktail, containing α-CD28 and α-CD3, for 48h (Figure 3E-H, Supplementary Figure 3B) before co-culturing them with melanoma cells. Additionally, to rule out any unspecific and/or toxic effect induced by the ASOs, we performed *LISR* KD with siRNAs (Figure 3F). Again, we could detect an early increase in PBMCs proliferation (Supplementary Figure 3B) and increased melanoma cell killing (Figure 3E-H) upon *LISR* targeting. To rule out that immune cell activation is not primed by secretion of soluble factors, we treated PBMCs with conditioned medium derived from M099 melanoma cultures. This did not stimulate PBMCs proliferation/activation (Supplementary Figure 3C-D). Accordingly, blocking of MHCI and MHCII with monoclonal antibodies before exposure to HLA-matched PBMCs significantly reduced cell death, indicating that the increase in cancer cell killing upon *LISR* KD is antigen-dependent (Supplementary Figure 3E).

Cytotoxic T cells are important effectors in anti-tumour immunity. Although this function has conventionally been ascribed to $CD8^+$ cells, intratumoral $CD4^+$ with cytotoxic activity have been recently identified [34].

Analysis of the number of $CD8^+$ and $CD4^+$ T cells by immunofluorescence upon *LISR* inhibition show a trend towards the increase in the amount of $CD8^+$ and the $CD8^+/CD4^+$ ratio (Figure 3I-K). Therefore, to further assess the role of $CD8^+$ and $CD4^+$ T cells in melanoma cell killing, we isolated $CD4^+$ and $CD8^+$ T cells subpopulations from HLA matched PBMCs and co-cultured them separately with

melanoma cells (Supplementary Figure 3F-G). In both cases we could detect Caspase-3 activation (Figure 3L-M) and reduced melanoma cell confluency (Supplementary Figure 3H-I) upon *LISR* KD, thus suggesting that both MHCI- and MHCII-dependent mechanisms of antigen presentation are at play. However, in $CD4^+$ co-cultures the number of caspase-positive cells was approximately half of what was observed in $CD8^+$-containing co-cultures unless co-treatment with α-PD1 was applied (Figure 3L-M). All together these results highlight the ability of *LISR* to protect melanoma cells from T-cell attack.

LISR regulates translation of selected mRNAs with immunoregulatory functions

To dissect the molecular mechanisms underlying *LISR*-dependent suppression of melanoma immunogenicity, we silenced this transcript (using a pool of siRNAs) (Figure 4A) and performed RNA sequencing. While 244 transcripts were significantly (adjusted $p<0.05$) dysregulated upon *LISR* KD, only four of them showed a $FC>|2|$, indicating that *LISR* KD caused only negligible changes in gene transcription. Gene Set Enrichment Analysis (GSEA; $p<0.05$ and $FDR<0.25$), nevertheless, suggested a role for *LISR* in the regulation of ribosome biogenesis and translation (Figure 4B). We therefore performed polysome profiling (Figure 4C) and RNA sequencing in *LISR* KD cells. About a fifth of the entire MM099 translatome was affected upon *LISR* silencing (Figure 4D). GSEA indicated a significant (nominal p-value=0,022) inverse correlation between the translatome regulated by *LISR* and mRNAs translated during activation of the ISR (Figure 4E). Particularly relevant was a decrease of ATF4 mRNA at polysomes (Supplementary Figure 4A), which resulted in a significant decrease of ATF4 protein levels as shown by western blot analysis (Figure 4F-G). Similar results

were obtained with RNaseH-mediated degradation of *LISR* (Supplementary Figure 4 B-D) and in another mesenchymal-like melanoma line (Supplementary Figure 4E-G). To further substantiate these findings, we built an ATF4-reporter system (pFULT-hCARS, Supplementary Figure 4H), in which the dt-Tomato and luciferase genes were placed under control of the human ATF4-responsive CARS promoter [35]. The reporter system was introduced into a PDX-derived melanoma cell line (Mel-015). As expected salubrinal exposure led to a robust activation of the reporter in cells transfected with non-targeting siRNAs (Ctrl). In contrast, co-transfection with *LISR*-targeting siRNAs (si*LISR*) led to a significant decrease in luciferase and fluorescent reporter activity (Figure 4H-I and Supplementary Figure 4I).

The further mining of our polysome profiling sequencing dataset highlighted three additional important findings.

First, the two lncRNAs outlined in figure1F-H, and whose translation was repressed upon ISR activation, were enriched at polysomes upon *LISR* KD (Figure 4J-K). Importantly, Immune Epitope Database tool (IEDB: http://tools.iedb.org/main/) predicted that both lncRNA-encoded peptides may actually be ligands of MHCI and II (Supplementary Table 2), and thereby function as putative neoantigens.

Second, translation of *PD-L1* was also found to be dependent on *LISR*. LISR KD decreased *PD-L1* mRNA expression and early polysome occupancy in ISR-activated cells (Supplementary Figure 4J).

Third, GSEA analysis revealed a translational downregulation (p-value<0.05; FDR-val<0.25) of genes involved in the biosynthesis and metabolism of glycolipids and glycoproteins upon *LISR* KD (Figure 5A). This was further confirmed by the decrease in O-GlcNac detected by western blotting in MM099 transfected with an siRNA against *LISR* (Figure 5B-C) or with a *LISR*-targeting ASO (Supplementary Figure 4K-

L). Similar results were obtained with MM165, another mesenchymal-like melanoma line (Supplementary Figure 4M-N). Additionally, co-staining for the MHCII and O-GlcNac revealed an overlap between the glycosylation signal and the antigen presenting machinery (Figure 5E-F). Given the previously reported negative association between the built up of the glycocalyx and immunogenicity of tumours [36], these data raise the possibility that *LISR* may promote immune evasion by inducing the presentation of sugars at the surface of cancer cells.

These data suggest that *LISR* recruitment to polysomes in cells undergoing ISR activation facilitates the translation of selective transcripts, such as PD-L1 and genes involved in biosynthesis and metabolism of glycans, while suppressing the production of potential neoantigens derived from annotated lncRNAs. Together, these data provide mechanistic insights into how *LISR* regulates melanoma immunogenicity.

Systemic inhibition of LISR affects immune responses *in vivo* and re-sensitizes to α-PD1 therapy

To assess clinical relevance of these findings *in vivo*, we engrafted a PDX melanoma model resistant to immunotherapy into immunocompromised mice (NOG) as well as into mice humanised with $CD34^+$ hematopoietic stem cells (hu-NOG; Supplementary Figure 5A). Systemic inhibition of *LISR* by subcutaneous injection of an ASO in tumour-bearing immune compromised mice (Figure 6A) did not affect overall survival (Figure 6B), indicating that *LISR* KD is *per se* not required for the *in vivo* growth of melanoma cells. In humanised mice, however, the same treatment significant delayed tumour growth (Figure 6C) and resulted in a significant increase in overall survival (Figure 6B). Critically, *LISR* targeting re-sensitized this PDX model to ICB (Figure 6D).

Western blot for O-linked N-acetylglucosamine confirmed its downregulation *in vivo* upon pharmacological inhibition of *LISR* (Supplementary Figure 5B-C).

To further study the molecular and cellular consequences of *LISR* KD *in vivo*, we profiled the melanoma lesions using a highly sensitive spatial transcriptomics method (Molecular cartography, resolve Biosciences). This analysis confirmed the successful targeting of *LISR* (Figure 6E) and revealed that *LISR* KD profoundly affects melanoma heterogeneity (Figure 6F), by significantly reducing the amount of several drug-tolerant subpopulations, including the NCSC. Increased infiltration of T, B and myeloid cells was also detected (Figure 6G), together with a decrease in regulatory T cells (T_{reg}) and T cell exhaustion markers (Figure 6G). Strikingly, staining of the glycans with lectins also revealed a clear decrease in their exposure on the glycocalyx upon *LISR* KD *in vivo* (Figure 6H).

These data provide a proof of concept that inhibition of LISR re-sensitises to ICB.

Discussion

We describe herein a role for *LISR* as a critical regulator of melanoma immunogenicity. We show that this non-coding transcript is widely expressed in cancer/melanoma cells, but not in normal cells, to promote an immune-tolerant translatome. While evidence of specific ribosomal proteins contributing to ribosome heterogeneity continue to emerge [37], our data provide evidence that tailor-made ribosomes can be obtained also by incorporating individual lncRNAs into the ribosome. The incorporation of *LISR* into polysomes during the ISR generates cancer-specific ribosome and contribute to the emergence of DTPCs. Mechanistically, the retention of *LISR* at polysomes prevents the production of peptides from two other lncRNAs, thereby suppressing a potential alternative source of neoantigens beyond standard tumor specific mutations. There is

indeed increasing evidence that expression of peptides from non-coding genes function as potential tumor neoantigens [38]. *LISR* recruitment at polysomes also favours translation of mRNAs with immunosuppressive functions, such as that encoding for the immune checkpoint receptor PD-L1 and several enzymes implicated in the formation of the glycocalyx. This carbohydrate sugar coat acts as a physical barrier to protect cancer cells from immune recognition and attack [39]. Its aberrant composition is an hallmark of cancer and currently used as predictive biomarkers [40]. Analogs have been designed to target glycosylation, however, given their limited uptake by the cells, these inhibitors are of limited therapeutic benefit. Our data offer an alternative, clinically compatible, approach to target this pathway in a cancer cell-specific manner. Consistently, we show that targeting *LISR* sensitizes refractory melanoma to immune checkpoint blockade. Given that LISR copy number and expression are increased in many different cancer types, we surmise that this approach may be applicable beyond melanoma.

From a fundamental point of view, our data support a model in which a single cancer cell-specific lncRNA, namely *LISR*, can participate to the assembly of specialized cancer ribosomes to promote immune evasion and thereby tumor progression and resistance to immunotherapy. Moreover, since LISR is primate-specific, this study provides yet another example of non-conserved transcript that contribute to the development of a human disease. Conservation has long been used to imply functionality of lncRNAs [41] and this has led to a bias in the recognition of important (non-)coding drivers in cancer [42]. However, since cancer cells are exposed to a much higher selective pressure compared to normal cells, especially when exposed to therapeutic pressure, it is reasonable to assume that these cells may evolve *de*

novo survival mechanisms that involve portions of the genome that are not necessarily functional in normal cells [43].

Material and methods

Cell lines and transfection

SKMEL-28 (from ATCC) were grown in RPMI 1640 (Gibco BRL Invitrogen), supplemented with 10% FBS (Gibco BRL Invitrogen) and 1% penicillin/streptomycin (Sigma-Aldrich). The patient-derived low-passage MM cell lines (a gift from G.-E. Ghanem) were grown in F-10 (Gibco BRL Invitrogen), supplemented with 10% FBS (Gibco BRL Invitrogen) and 1% penicillin/streptomycin.

All cell lines used are of human origin and were confirmed negative for mycoplasma before experimental use by using the MycoAlert Mycoplasma Detection Kit (Lonza) according to the manufacturer's specifications.

Gender of the patients from whom the cell cultures were derived is as follows (female: F; male: M): SK-MEL-28, M; MM034, F; and MM011, F; MM099, M; MM165, M; MM001, F; MM074, F; MM087, F; A375, F; MM031, M; MM162, M; MM047, M; MM057, F; MM163, F; MM052, M; MM029, M.

For ATF4 knock-down, SKMEL-28, MM099 and MM029 were plated in 6-well plates and transfected with Lipofectamine 2000 (Thermo Fisher Scientific) according to manufacturer instructions either with 25 nM non-targeting siRNA control or with targeting siRNA (SMART-pool, Dharmacon) 24h after seeding. For *LISR* KD either control (MISSION® siRNA Universal Negative Control #1 and #2, Sigma Aldrich) or si*LISR* (Sigma Aldrich, for sequences refer to Table S1) were used at a concentration of 25 nM. For ASO-mediated KD the ASO against LISR (Table S2) or a non-targeting

control (Table S2) were used at a final concentration of 50 nM. Cells were collected for RNA and protein extraction 48h after transfection.

ASO synthesis

Antisense oligonucleotides synthesis was performed on an Expedite 8909 DNA synthesiser (Applied Biosystems) by using the phosphoramidite method. The oligomers in the form of phosphorothioated LNA GapmeRs were deprotected and cleaved from the solid support by treatment with AMA solution (1:1 mixture of ammonia 33% and methylamine 40%) for 2h at 40°C. After gel filtration on an illustra NAP-25 column (Sephadex G-25 DNA Grade; GE Healthcare) using water as an eluent, the crude mixture was purified using a MonoQ HR 10/100 GL anion exchange column (GE Healthcare) with the following gradient system: 10 mM $NaClO_4$ and 20 mM Tris-HCl in 15% CH_3CN, pH 7.4 (A); 600 mM $NaClO_4$ and 20 mM Tris-HCl in 15% CH_3CN, pH 7.4 (B), 0-80% buffer B in 40 min, 2 mL/min. The low-pressure liquid chromatography system consisted of a Primaide PM1110 HPLC pump, Mono-Q HR 10/100 GL column, and Primaide PM1410 HPLC UV detector. The product-containing fractions were desalted on a NAP-25 column and lyophilized, and ASO sequences were analysed by mass spectrometry.

Coculture experiment

Upon knock-down of *LISR*, MM099 were cocultured with HLA matched PBMCs (Precision for medicine) at 1:5 ratio. MM099 were seeded in a 96 well and transfected 24h after using lipofectamine LTX (Thermo Fisher Scientific), according to manufacturer instruction. Pre-activated PBMCs were added 48h post transfection and the cocultures were followed for up to 120h.

To activate the T cells, freshly thawed PBMCs were cultured in RPMI 1640 (Gibco BRL Invitrogen), supplemented with 10% FBS (Gibco BRL Invitrogen) and 1% penicillin/streptomycin (Sigma-Aldrich) and 3 µg/ml of human α-CD3 (Thermo Fisher Scientific), 5 µg/ml of human α-CD28 (Thermo Fisher Scientific), and 200 ng of IL-2 (Immunotools) for 48h before coculturing them with melanoma cells.

Cocultures were monitored by use of IncuCyte ZOOM system (Essen BioScience), four images per well were taken every 2h. PBMCs were labelled with 1:1000 Incucyte® Nuclight Rapid Red Dye for Live-Cell Nuclear Labeling Incucyte (Sartorius) while cells death was measured by adding the IncuCyte Caspase 3/7 Green Apoptosis Assay Reagent 1:5000 to the cocultures (Essen BioScience). The cell confluency and caspase positivity were measured and analyzed with IncuCyte ZOOM software. The same experiment was performed with the same settings using ASOs.

In order to block MHC I or MHC II, MM099 were cultured with α-human MHC class I HLA-A, HLA-B, HLA-C (#78792101, clone W6/32; inVivoMab™) or α-human MHC class II HLA-DP/DQ/DR (#47AU4, clone IVA12; antibodies online) at a final concentration of 10 µg/ml before seeding. After 48h, the antibodies were refreshed by supplementing the media with an additional 10 µg/ml of either one or the other.

Polysome profiling

Melanoma cells for polysome profiling were plated in order to obtain a confluency of 70% on the day of the experiment. MM099 (plated in 15 cm dishes, 2 per condition) were transfected using lipofectamine 2000 (Thermo Fisher Scientific), according to manufacturer instruction, either with 25 nM sipool control (MISSION® siRNA Universal Negative Control #1 and #2, Sigma Aldrich) or with 25 nM of sipool for LISR (Sigma Aldrich, for sequences refer to table) for 48h. At endpoints, cells were treated with 100

µg/ml of cycloheximide (Sigma-Aldrich) for 12 min at 37°C, collected, and resuspended in lysis buffer 2 [20 mM Trish-HCl pH 7.4, 10 mM NaCl, 3 mM MgCl2 supplemented with 1.2% TRITONX-100, 0.2 M Sucrose, 100 µg/ml cycloheximide, 20 U/µl SUPERase-IN RNase Inhibitor (Invitrogen, Thermo Fisher Scientific), supplemented with fresh 1× Halt Protease and Phosphatase Inhibitor Single-Use Cocktail (Life Technologies). Lysates were then incubated agitating at 4°C for 35min, and then centrifuged at 17,000 rcf for 15 min at 4°C. Lysates were loaded on a sucrose gradient (15%-50%) prepared in buffer G (20 mM Tris- HCl, 100 mM KCl, 10 mM MgCl2 supplemented with 1 mM DTT (Sigma Aldrich) supplemented with fresh 100 µg/ml cycloheximide. Samples were then centrifugated in an SW41Ti rotor (Beckman Coulter) at 37,000 rpm at 4°C for 150 min. The fractions were obtained with a Biological LP System (Bio-Rad). A total of 14 (600 µl) fractions were collected per sample and pulled together to obtain clean 40S, 60S, 80S, and polysomes.

Polysome profiling of PDX-derived samples, was performed as previously described [23] with minor adjustments. Samples homogenized in lysis buffer were loaded onto a 5%-20% linear gradient and centrifugated at 37,000 rpm for 170 min at 4°C in an SW41Ti rotor (Beckman Coulter).

MS-based proteomics analysis

Both control and salubrinal-treated cell pellets were digested using the PreOmics iST sample preparation kit, following the manufacturer's guidelines. In all cases, proteolytic peptides were separated by reversed-phase chromatography on an EASY-nLC 1200 ultra-high-performance liquid chromatography (UHPLC) system through an EASY-Spray column (Thermo Fisher Scientific), 25-cm long (inner diameter 75 µm, PepMap C18, 2 µm particles), which was connected online to a Q Exactive HF (Thermo Fisher

Scientific) instrument through an EASY-Spray™ Ion Source (Thermo Fisher Scientific). Both for library and study samples, the purified peptides were loaded in buffer A (0.1% formic acid in water) at constant pressure of 980 Bar. They were separated through the following gradient: 30 min of 3-23% of buffer B (0.1% formic acid, 80% acetonitrile), 5 min 23-30% of buffer B, 1 min 60-95% buffer B, at a constant flow rate of 250 nl/min. The column temperature was kept at 45°C under EASY-Spray oven control. The mass spectrometer was operated data-dependent acquisition (DDA) mode. Briefly, MS spectra were collected in the Orbitrap mass analyzer at a 60,000 resolution (200 m/z) within a range of 300–1550 m/z with an automatic gain control (AGC) target of 3e6 and a maximum ion injection time of 20 ms. The 15 most intense ions from the full scan were sequentially fragmented with an isolation width of 1.4 m/z, following higher-energy collisional dissociation (HCD) with a normalized collision energy (NCE) of 28%. The resolution used for MS/MS spectra collection in the Orbitrap was 15,000 at 200 m/z with an AGC target of 1e5 and a maximum ion injection time of 80 ms. Precursor dynamic exclusion was enabled with a duration value of 20s. MS Raw files were processed with MaxQuant (MQ) version 2.0.3.0 integrated with Andromeda search engine. Sequenced non-coding RNAs were in silico translated into amino acid sequences already in FASTA format, using the “Six-frame translation” tool available in the MQ suite. In parallel, MSMS spectra were also searched against the human reference proteomes (Uniprot UP000005640, 80,027 entries). The search included cysteine carbamidomethylation as a fixed modification and methionine oxidation and acetylation of the protein N-terminus as variable modifications. Required minimum peptide length was 7 amino acids and maximum mass tolerances were 4.5 p.p.m. for precursor ions after nonlinear recalibration and 20 p.p.m. for fragment ions.

Identifications were stringently filtered for a FDR < 1% at both peptide spectrum match and protein group levels.

RNA extraction

For RNA extraction of ribosomal fractions, each fraction was digested at 37°C for 90 min in a mix of proteinase K (final concentration 100 µg/ml; Sigma-Aldrich) and 1% SDS. Phenol acid chloroform (5:1; Sigma-Aldrich) and 10mM NaCl were then added. Samples were centrifuged at 16,000 rcf for 5 min at 4°C. The upper aqueous phase was transferred to a new tube, and 1 ml of isopropanol was added. Samples were stored at −80°C overnight to precipitate the RNA. The following day, the samples were centrifuged at 16,000 rcf for 40 min at 4°C. The supernatant was discarded, and the pellet was washed with 500 µl of 70% EtOH, then centrifuged again at 16,000 rcf for 5 min at 4°C. Pellet were air dried and resuspended in nuclease-free water. For all the other uses, RNA was extracted with TRIzol (Invitrogen) and subjected to DNase treatment using TURBO DNA-free™ Kit (Invitrogen) according to manufacturer's instructions.

RT and qPCR

RNA was reverse transcribed using the High-Capacity complementary DNA Reverse Transcription Kit (Thermo Fisher Scientific) on a Veriti 96-well thermal cycler (Thermo Fisher Scientific). Gene expression was measured by qPCR on a QuantStudio 5 (Thermo Fisher Scientific) and normalized with ΔΔCt method using 28S and 18S as reference genes (for polysome profiling experiments) or on the average of GAPDH, UBC, and βActin. Sequences of the primers are indicated in Table S3.

For the evaluation of lncRNA polyadenylation total RNA was reverse transcribed with the High-Capacity complementary DNA Reverse Transcription Kit (Thermo Fisher Scientific) using either random hexamers or Oligo(dT)12-18 Primer (Thermo Fisher Scientific), on a Veriti 96-well thermal cycler (Thermo Fisher Scientific). Polyadenylation was measured by qPCR on a QuantStudio 5 (Thermo Fisher Scientific) and normalized with ΔΔCt method using transcript-specific primers. GAPDH, UBC, and βActin as reference genes Sequences of the primers are indicated in Table.

RNA sequencing and data analysis

Samples were prepared for sequencing using TruSeq Stranded Total RNA kit (Illumina) according to the manufacturer's instructions. Libraries were sequenced on an Illumina NextSeq and HiSeq4000 according to the manufacturer's instructions, generating PE high output configuration cycles: (R1: 100) − (I1: 6) − (I2: 0) − (R2: 100) and (R1: 50) − (I1: 6) − (I2: 0) − (R2: 0). Differential gene expression analysis was performed as previously described [23].

Nuclear fractionation

Melanoma cells were plated in 15 cm dishes and treated with 20 μM Salubrinal (Sigma-Aldrich) for 72 h. At endpoint, cells were washed 2x with cold PBS (Gibco BRL Invitrogen), and then collected in 1,5 ml of Nuclei EZ lysis buffer (Sigma Aldrich) supplemented with 20 U/μl SUPERase-IN RNase Inhibitor (Invitrogen, Thermo Fisher Scientific), 1× Halt Protease and Phosphatase Inhibitor Single-Use Cocktail (Life Technologies) and 1 mM DTT (Sigma Aldrich). Cell lysate was thoroughly vortexed 8 times, then incubated 15 minutes on ice and centrifuged at 500 rcf for 5 minutes at 4

°C. Pellet was washed with 1,5 ml of of Nuclei EZ lysis buffer (Sigma Aldrich) supplemented with 20 U/µl SUPERase-IN RNase Inhibitor (Invitrogen, Thermo Fisher Scientific), 1× Halt Protease and Phosphatase Inhibitor Single-Use Cocktail (Life Technologies) and 1 mM DTT (Sigma Aldrich), vortexed, incubated on ice for 10 minutes on ice and centrifugated at 500 rcf for 5 minutes at 4 °C. This step was repeated once, excluding the incubation on ice. The lysate was then divided in 2 for protein extraction and RNA extraction for further analysis. Nuclear enrichment was validated by RT-qPCR and by western blot.

Protein extraction and western blot

Proteins were extracted resuspending cellular pellet in RIPA buffer [150 mM NaCl, 50 mM Tris-HCl pH 8, 1% Nonidet P40 (Thermo Fisher Scientific), 0.5% Sodium Deoxycholate (Sigma Aldrich), 1mM EDTA (Sigma Aldrich)] supplemented with 1× Halt Protease and Phosphatase Inhibitor Single-Use Cocktail (Life Technologies).

Western blotting experiments were performed using the following primary antibodies at the indicated dilution: vinculin (V9131, clone VIN-1; Sigma-Aldrich, 1:5,000), MITF (ab12039; Abcam, 1:1,000), ATF4 (#11815, clone D4B8; Cell Signaling Technology, 1:500), eIF2α-Tot (#5324, clone D7D3; Cell Signaling Technology, 1:1,000), eIF2α-Phospho-S51 (#3398, clone D9G8; Cell Signaling Technology, 1:800), α-O-Linked N-Acetylglucosamine (MABS157, clone RL2; Sigma Aldrich, 1:800), α-human MHC class I HLA-A, HLA-B, HLA-C (#78792101, clone W6/32; inVivoMab™, 1:1000), α-human MHC class II HLA-DP/DQ/DR (#47AU4, clone IVA12; antibodies online, 1:1000).

The following HRP-linked secondary antibodies were used: α-mouse IgG (NA931-1ML; Sigma-Aldrich, 1:5,000) and α-rabbit IgG (NA934-1ML; Sigma-Aldrich, 1:5,000). Relative protein levels were measured using ImageJ.

Immunofluorescence

For immunofluorescence, cells were grown either on Falcon® 8-well Culture Slide (Corning) or in PhenoPlate 96-well (Perkin Elmer), fixed in 3.7% formaldehyde for 20 minutes at RT and permeabilized in 1% BSA (Sigma-Aldrich) and 0.2% Triton X-100 (Sigma-Aldrich)-containing buffer for 10min on ice. Blocking was performed in 1% BSA and 10% goat serum (Abcam) for 30min at room temperature. Primary antibody incubation was performed at room temperature for 1h. For co-staining of multiple antigens, sequential staining with different primary antibodies was performed. To detect MHC class I, a mouse antibody (#78792101, clone W6/32) from inVivoMab™ was used at a concentration of 1:1000. To detect MHC class II, a mouse antibody (#47AU4, clone IVA12) from antibodies online was used at a concentration of 1:1000. To detect O-Linked N-Acetylglucosamine, a mouse antibody (MABS157, clone RL2) from Sigma Aldrich was used at a concentration of 1:1000. For double staining with these two antibodies, a sequential immunostaining protocol was used. To detect CD4, an antibody already labelled with FITC (130-113-775, clone REA623) from Miltenyi biotec was used at a concentration of 1:100. To detect CD8, an antibody already labelled with PE-Vio-770 (130-113-721, clone REA734) from Miltenyi biotec was used at a concentration of 1:100. Secondary antibody incubation was performed for 45 minutes at room temperature in the dark. As secondary antibodies, α-rabbit or α-mouse AlexaFluor-488 and AlexaFluor-647 (Life Technologies, 1:1,000) were used. Nuclei were stained with 1:1000 DAPI (Sigma Aldrich) for 15 minutes at room

temperature before mounting the slides with ProLong™ Glass Antifade mounting medium (Thermo Fisher Scientific). Slides were imaged using Nikon C2 confocal microscope while the 96 wells were imaged by the high content screening microscope Operetta CLS+ Twister (Perkin Elmer). Analysis was performed using Image J and Harmony software (Perkin Elmer). Colocalization analysis was performed using Fiji Image J plug-in JACoP; Van Steensel on a z-stack of confocal images. Evaluation of the level of colocalization was measured with Cross correlation function (CCF) with a pixel shift of $\delta = \pm 20$.

Fluorescent in situ hybridization

For detection of LISR, 8 FISH probes (IDT) (Table S3) marked with FAM were designed using the Stellaris probe designer software (Biosearch Technologies). Cells were grown either on Falcon® 8-well Culture Slide (Corning) or on round glass coverslips (VWR), fixed in 3.7% formaldehyde 10 minutes at RT and permeabilized in 70% EtOH for at least 1h at 4 °C. Cells were then washed twice with wash buffer (2×sodium lauryl sulfate, 10% formamide) and hybridized with 250 nM of pooled probes (for the sequences refer to table) in hybridization buffer (2×sodium lauryl sulfate, 10% formamide and 10% dextran) overnight at 37 °C.

Cells were washed with wash buffer for 30 minutes at 37°C, twice with PBS and mounted with Invitrogen™ ProLong™ Gold Antifade mounting media with 4,6-diamidino2-phenylindole (DAPI) (Thermo Fisher Scientific). Nikon C2 confocal microscope was used for visualization and analysis was performed on Image J.

PDX models

The cutaneous melanoma PDX models are part of the Trace collection (https://gbiomed.kuleuven.be/english/research/50488876/54502087/Trace) and were established using metastatic melanoma lesions derived from patients undergoing surgery as part of standard treatment at UZ Leuven. All patients were asked to sign a written informed consent and procedures involving human samples were approved by the UZ Leuven/KU Leuven Medical Ethical Committee (S63799). PDX models Mel-006, Mel-015, and Mel-020 were derived from a female, male, and female drug-naive patients, respectively. The UM Mel-077 sample was derived from a male patient progressing on pembrolizumab and temozolomide. Mel- 018, Mel-021, and Mel-078 were derived from male, female, and male patients, respectively. PDX models Mel-015, MEL058 and MEL029 are derived from male drug-naïve patients. PDX model MEL083 is derived from a male patient resistant to targeted and immunotherapy. All the PDX models were used in accordance with the principles of the Declaration of Helsinki and with GDPR regulations. All the animal experiments were approved by the KU Leuven animal ethical committee under ECD P164/2019, P210/2018 and P032/2022 and performed in accordance with the internal, national, and European guidelines of animal care and use. Mice were implanted with tumor pieces subcutaneously in the interscapular fat pad and maintained in a semi-specific pathogen–free facility under standard housing conditions with continuous access to food and water. The health and welfare of the animals was supervised by a designated veterinarian. The KU Leuven animal facilities comply with all appropriate standards (cages, space per animal, temperature [22°C], light, humidity, food, and water), and all cages are enriched with materials that allow the animals to exert their natural behavior. Mice used in the study were maintained on a diurnal 12-h light/dark cycle.

NOD/Shi-scid/IL-2Rγnull, engrafted at the age of 5 weeks with $CD34^+$ hematopoietic stem cells, isolated from 3 different donor cord blood, were provided by TransCure bioServices. Tumours were engrafted into humanized mice (23 weeks old) and treatment with ASO (15mg/kg sub cutaneous every second day) and/or nivolumab (10 mg/kg twice a week i.p.) was initiated when the tumor reached the size of 100 mm^3. The study was terminated when the mice reached 1.5mm^3.

The percentage of humanization was estimated by flow cytometry analysis for CD45+ cells 14 weeks after engraftment ad calculated as follows Humanization rate (%) = hCD45/(hCD45+mCD45)*100.

Mice engrafted with $CD34^+$ from the same donor where randomized in the different treatment groups. According to animal welfare guidelines, mice were sacrificed when tumors reached a volume of 1,500 mm3 or when body weight decreased >20% from the initial weight. Mice used in this study never reached or exceeded these limits.

ATF4 reporter

To generate the ATF4 inducible reporter, the human CARS promoter sequence (a known ATF4 target whose promoter contains a C/ebp-Atf response element [35]) was placed upstream of a luciferase-tdTomato transgene.

Specifically, the DNA sequence of the human CARS promoter (a DNA fragment of 518 bp upstream and 959 bp downstream of the human CARS TSS (ENSG00000110619, transcript ENST00000397111) was transferred from a pGL3.1 backbone (kind gift of Prof. Michael Kilberg, [35]) into a plasmid expressing both luciferase and tdTomato (pFULT, kind gift of Prof. Ghambir) using InFusion (Takara Bio) according to the manufacturer's specifications.

TCGA analysis

LISR RNA expression levels were quantified (Log2 normalised counts per million) in 175 melanoma patients using the UCSC Xena (https://xenabrowser.net/). Patients were split in two groups, proliferative (n= 82) and invasive (n=93) according to the criteria described in [32].

LISR copy number (Log2 normalised) was quantified in 473 melanoma patients (TCGA_SKCM) using the UCSC Xena (https://xenabrowser.net/).

Bulk RNA sequencing and GSEA

Raw FASTQ files downloaded from the GEO database [44] project "mRNA expressions in pre-treatment melanomas undergoing α-PD-1 checkpoint inhibition therapy" (data accessible at NCBI GEO database [33], accession GSE78220) or produced by the laboratory were passed through FASTQ Groomer [45]. Adaptors were trimmed and low-quality reads were discarded using Trimmomatic [46]. The reads were pseudo-aligned to the human reference genome GRCh38 [47] and counted using Kallisto [48]. The R package Sleuth [49] was used for normalization of the counts. was handled with the R package Seurat. The R packages ggpubr and ggplot were used to plot gene expression. Geneset enrichment analysis [50] was performed with GSEA 4.1.0 on the normalized counts. Plots visualizing GSEA data were made in R using the ggplot2 package [51] and only genesets with nominal p-value < 0.05 and FDR q-value < 0.25 are shown.

Single cell RNA seq

The single cell sequencing data from human melanoma patients before and after a single dose of ICB therapy [32] was handled with the R package Seurat. The R packages ggpubr and ggplot [51] were used to plot gene expression from this dataset.

Molecular Cartography

Probe Design

The probes for 100 genes were designed at the gene-level using Resolve's proprietary design algorithm. For every targeted gene all full-length transcript sequences from the ENSEMBL database were used as design targets if the isoform had the GENCODE annotation tag 'basic' [52, 53]. To filter highly repetitive regions, the abundance of k-mers was obtained from the background transcriptome using Jellyfish [54]. Every target sequence was scanned once for all k-mers, and those regions with rare k-mers were preferred as seeds for full probe design. A probe candidate was generated by extending a seed sequence until a certain target stability was reached. A set of simple rules was applied to discard sequences that were found experimentally to cause problems. After these fast screens, every kept probe candidate was mapped to the background transcriptome using ThermonucleotideBLAST [55] and probes with stable off-target hits were discarded. Specific probes were then scored based on the number of on-target matches (isoforms), which were weighted by their associated APPRIS level [56], favoring principal isoforms over others. From the pool of accepted probes, the final set was composed by greedily picking the highest scoring probes. Gene and probes ID are provided in Supplementary Table 3.

Sample preparation

Freshly dissected humanized PDX tumours (3 per treatment cohort) were frozen in isopentyne (Fisher Scientific) and sectioned with a cryostat HM 525 NX (Thermo Fisher) and 10µm thick sections were placed within the capture areas of cold Resolve Biosciences slides. Samples were then sent to Resolve BioSciences on dry ice for analysis. Upon arrival, mouse tissue sections were thawed and fixed with 4% v/v Formaldehyde (Sigma-Aldrich F8775) in 1x PBS for 20 min at 4 °C, whereas the human samples were fixed for 45min at 4 °C. After fixation, sections were washed twice in 1x PBS for two min, followed by one min washes in 50% Ethanol and 70% Ethanol at room temperature. Fixed samples were used for Molecular Cartography™ (100-plex combinatorial single molecule fluorescence in-situ hybridization) according to the manufacturer's instructions as previously described [57]. A total of 50 tiles per sample were imaged.

Imaging

Samples were imaged on a Zeiss Celldiscoverer 7, using the 50x Plan Apochromat water immersion objective with an NA of 1.2 and the 0.5x magnification changer, resulting in a 25x final magnification. Standard CD7 LED excitation light source, filters,

and dichroic mirrors were used together with customized emission filters optimized for detecting specific signals. Excitation time per image was 1000 ms for each channel (DAPI was 20 ms). A z-stack was taken at each region with a distance per z-slice according to the Nyquist-Shannon sampling theorem. The custom CD7 CMOS camera (Zeiss Axiocam Mono 712, 3.45 µm pixel size) was used. For each region, a z-stack per fluorescent color (two colors) was imaged per imaging round. A total of 8 imaging rounds were done for each position, resulting in 16 z-stacks per region. The completely automated imaging process per round (including water immersion generation and precise relocation of regions to image in all three dimensions) was realized by a custom python script using the scripting API of the Zeiss ZEN software (Open application development).

Spot Segmentation

The algorithms for spot segmentation were written in Java and are based on the ImageJ library functionalities. Only the iterative closest point algorithm is written in C++ based on the libpointmatcher library (https://github.com/ethz-asl/libpointmatcher).

Pre-processing

As a first step all images were corrected for background fluorescence. A target value for the allowed number of maxima was determined based upon the area of the slice in µm² multiplied by the factor 0.5. This factor was empirically optimized. The brightest maxima per plane were determined, based upon an empirically optimized threshold. The number and location of the respective maxima was stored. This procedure was done for every image slice independently. Maxima that did not have a neighboring maximum in an adjacent slice (called z-group) were excluded. The resulting maxima list was further filtered in an iterative loop by adjusting the allowed thresholds for (Babs-Bback) and (Bperi-Bback) to reach a feature target value (Babs: absolute brightness, Bback: local background, Bperi: background of periphery within 1 pixel). This feature target values were based upon the volume of the 3D-image. Only maxima still in a zgroup of at least 2 after filtering were passing the filter step. Each z-group was counted as one hit. The members of the z-groups with the highest absolute brightness were used as features and written to a file. They resemble a 3D-point cloud. Final signal segmentation and decoding: To align the raw data images from different imaging rounds, images had to be corrected. To do so the extracted feature point clouds were used to find the transformation matrices. For this purpose, an iterative closest point cloud algorithm was used to minimize the error between two point-clouds.

The point clouds of each round were aligned to the point cloud of round one (reference point cloud). The corresponding point clouds were stored for downstream processes. Based upon the transformation matrices the corresponding images were processed by a rigid transformation using trilinear interpolation. The aligned images were used to create a profile for each pixel consisting of 16 values (16 images from two color channels in 8 imaging rounds). The pixel profiles were filtered for variance from zero normalized by total brightness of all pixels in the profile. Matched pixel profiles with the highest score were assigned as an ID to the pixel. Pixels with neighbors having the same ID were grouped. The pixel groups were filtered by group size, number of direct adjacent pixels in group, number of dimensions with size of two pixels. The local 3D-maxima of the groups were determined as potential final transcript locations. Maxima were filtered by number of maxima in the raw data images where a maximum was expected. Remaining maxima were further evaluated by the fit to the corresponding code. The remaining maxima were written to the results file and considered to resemble transcripts of the corresponding gene. The ratio of signals matching to codes used in the experiment and signals matching to codes not used in the experiment were used as estimation for specificity (false positives).

Downstream analysis

For the analysis, cell segmentation was performed with the Automatic Cell Segmentation tool provided by Resolve based on DAPI images. Pixels are burred at tiling gaps in the DAPI panorama images to migitate over-segmentation due to artificial borders at the edges of field of views with costum software called MindaGap at default settings MindaGap is available at https://github.com/ViriatoII/MindaGap. Subsequently, Cellpose [58] was used to segment the cell nuclei in the pre-trained cyto model with diameter and flow-thresh parameters set to 50.0 and 0.5, respectively. Compartment specific genes were determined by calculating the ratio of total transcript counts and transcripts inside DAPI segments per gene. Genes having >=70% of transcripts located inside DAPI segments are considered nucleus specific, genes with <=30% of transcripts in DAPI segments are considered cytoplasmic. Cells were segmented based on transcript coordinates using Baysor [Petukhov et al. 2021] with DAPI segments as prior and the following parameter settings: --no-ncv-estimation --force-2d --n-clusters=1 --prior-segmentation-confidence 0.9 -m 3. Baysor's

compartment genes feature was used by adding genes matching the above-mentioned compartment definitions to Baysor's --nuclei-genes and --cyto-genes parameters, respectively. Finally, the outline of cells was predicted by Baysor by running the convex hull algorithm on the corresponding subset of transcripts assigned to each individual cell. The R package Seurat was used to normalize and integrate the count matrices into one dataset. Cells that expressed less than two genes were filtered out and cell states were assigned using the R package AUCell with the gene markers listed in Supplementary table 3. Gene expression of different immune cells markers (Supplementary table 3) and lncRNAs were plotted with the R packages ggpubr and ggplot [51].

WGA staining

Existing solution was discarded and HBSS was used to wash the slides twice for 1min. The solution was aspirated and discarded. Glycans were stained with Wheat Germ Agglutinin, Alexa Fluor™ 633 Conjugate as previously described [59].

CCLE

LISR TPM counts were plotted for cutaneous melanoma cell lines from the CCLE [60] Sanger GDSC1 dataset [61] and correlated (Pearson correlation coefficient) with AUC of BRAF and MEK inhibitors dabrafenib and trametinib.

CPC2

Illumina reads were passed through FASTQ Groomer [45]. Adaptors were trimmed and low-quality reads were discarded using Trimmomatic [46]. The reads were pseudo-aligned to the human reference genome GRCh38 [47] and counted using Kallisto [48]. The R package Sleuth [49] was used for differential transcript expression analysis. The coding potential of the differentially expressed transcripts (FDR<0.05 & average control on average salubrinal <0.5 or >2) were predicted by CPC2 [62]. The R package ggplot2 [51] was used for making the figures.

Author's contributions

SC performed most of the in vitro wet lab experiments and assembled figures. YV performed all the bioinformatic analysis. ACC provided support for bulk RNAseq analysis. VK performed the experiments with pFULT-hCARS reporter. RV designed and built the pFULT-hCARS reporter. ED, FV, FS performed PDX experiments. MFB coordinated the *in vivo* work and analyzed the resulting data. EG provided ASO. OB provided access to essential human clinical samples and data. SA prepared samples for Molecular cartography and smFISH. JP provided access to essential human single-cell RNAseq data. ST provided analysis of mouse humanization. SH performed the experiments on MM0165. TB and AC designed, performed and interpreted mass spectrometry experiments. EL designed the study, interpreted the data and wrote the manuscript. All authors read and edited the manuscript.

Acknowledgment

We would like to thank the Light Microscopy and Imaging Network - LiMoNe (VIB-KULeuven), especially Axelle Kerstens, for the excellent technical support. We would also like to thank Dr K. De Keersmaecker and Dr J-C Marine for critical reading of the manuscript. We would like to thank Guy Schepers and Frédérick Coosemans (Rega Institute) for the excellent technical support. The present study was funded by a KU Leuven C1 grant, a Belgian federation for Cancer grant (FAF-F/2018/1184). E. Leucci is funded by the Melanoma Research Alliance Amanda and Jonathan Eilian young investigator award. Trace staff was supported by Stichting Tegen Kanker grant 2016-054. T. Bonaldi is supported by the Italian Association for Cancer Research grant number IG-2018-21834. This work has been supported by EPIC-XS, project number 823839, funded by the Horizon 2020 programme of the European Union. V. Katopodi

is a recipient of a FWO – Flanders research organization PhD fellowship (1S47519N). Y. Verheyden is FWO – Flanders research organization PhD fellowship (1SC5122N). S. Cinque is a recipient of FWO – Flanders research organization PhD fellowship (1SD1620N).

Conflict of Interest

The authors declare the following competing interests: Eleonora Leucci is inventor of the patent EP22174555.7 submitted on April 20th 2022 for the use of LISR KD for the treatment of melanoma.

References

1. Marine, J.C., S.J. Dawson, and M.A. Dawson, *Non-genetic mechanisms of therapeutic resistance in cancer.* Nat Rev Cancer, 2020. **20**(12): p. 743-756.
2. English, A.M., K.M. Green, and S.L. Moon, *A (dis)integrated stress response: Genetic diseases of eIF2α regulators.* Wiley Interdiscip Rev RNA, 2022. **13**(3): p. e1689.
3. Vivas-García, Y., et al., *Lineage-Restricted Regulation of SCD and Fatty Acid Saturation by MITF Controls Melanoma Phenotypic Plasticity.* Mol Cell, 2020. **77**(1): p. 120-137.e9.
4. Gay, D.M., A.H. Lund, and M.D. Jansson, *Translational control through ribosome heterogeneity and functional specialization.* Trends Biochem Sci, 2022. **47**(1): p. 66-81.
5. van Heesch, S., et al., *Extensive localization of long noncoding RNAs to the cytosol and mono- and polyribosomal complexes.* Genome Biol, 2014. **15**(1): p. R6.
6. Ingolia, N.T., et al., *Ribosome profiling reveals pervasive translation outside of annotated protein-coding genes.* Cell Rep, 2014. **8**(5): p. 1365-79.
7. Ruiz-Orera, J., et al., *Long non-coding RNAs as a source of new peptides.* Elife, 2014. **3**: p. e03523.
8. Aspden, J.L., et al., *Extensive translation of small Open Reading Frames revealed by Poly-Ribo-Seq.* Elife, 2014. **3**: p. e03528.
9. Vendramin, R., et al., *SAMMSON fosters cancer cell fitness by concertedly enhancing mitochondrial and cytosolic translation.* Nat Struct Mol Biol, 2018. **25**(11): p. 1035-1046.
10. Melixetian, M., et al., *Long non-coding RNA TINCR suppresses metastatic melanoma dissemination by preventing ATF4 translation.* EMBO Rep, 2021. **22**(3): p. e50852.
11. Yoon, J.H., et al., *LincRNA-p21 suppresses target mRNA translation.* Mol Cell, 2012. **47**(4): p. 648-55.
12. Prensner, J.R., et al., *Noncanonical open reading frames encode functional proteins essential for cancer cell survival*, in *Nat Biotechnol*. 2021. p. 697-704.
13. Calviello, L., A. Hirsekorn, and U. Ohler, *Quantification of translation uncovers the functions of the alternative transcriptome.* Nat Struct Mol Biol, 2020. **27**(8): p. 717-725.
14. Othoum, G., et al., *Pan-cancer proteogenomic analysis reveals long and circular noncoding RNAs encoding peptides.* NAR Cancer, 2020. **2**(3): p. zcaa015.
15. Chong, C., et al., *Integrated proteogenomic deep sequencing and analytics accurately identify non-canonical peptides in tumor immunopeptidomes.* Nature Communications, 2020. **11**(1): p. 1293.
16. Bi, P., et al., *Control of muscle formation by the fusogenic micropeptide myomixer.* Science, 2017. **356**(6335): p. 323-327.
17. Anderson, K.M., et al., *Transcription of the non-coding RNA upperhand controls Hand2 expression and heart development.* Nature, 2016. **539**(7629): p. 433-436.
18. Gaertner, B., et al., *A human ESC-based screen identifies a role for the translated lncRNA LINC00261 in pancreatic endocrine differentiation.* Elife, 2020. **9**.
19. Genuth, N.R. and M. Barna, *The Discovery of Ribosome Heterogeneity and Its Implications for Gene Regulation and Organismal Life.* Mol Cell, 2018. **71**(3): p. 364-374.
20. Barna, M., et al., *The promises and pitfalls of specialized ribosomes.* Mol Cell, 2022. **82**(12): p. 2179-2184.

21. Licari, E., L. Sánchez-del-Campo, and P. Falletta, *The two faces of the Integrated Stress Response in cancer progression and therapeutic strategies.* The International Journal of Biochemistry & Cell Biology, 2021. **139**: p. 106059.
22. Falletta, P., et al., *Translation reprogramming is an evolutionarily conserved driver of phenotypic plasticity and therapeutic resistance in melanoma.* Genes Dev, 2017. **31**(1): p. 18-33.
23. Vendramin, R., et al., *Activation of the integrated stress response confers vulnerability to mitoribosome-targeting antibiotics in melanoma.* J Exp Med, 2021. **218**(9).
24. Xu, Y., et al., *Translation control of the immune checkpoint in cancer and its therapeutic targeting.* Nat Med, 2019. **25**(2): p. 301-311.
25. Cerezo, M., et al., *Translational control of tumor immune escape via the eIF4F-STAT1-PD-L1 axis in melanoma.* Nat Med, 2018. **24**(12): p. 1877-1886.
26. Suresh, S., et al., *eIF5B drives integrated stress response-dependent translation of PD-L1 in lung cancer.* Nature Cancer, 2020. **1**(5): p. 533-545.
27. Kalaora, S., et al., *Mechanisms of immune activation and regulation: lessons from melanoma.* Nat Rev Cancer, 2022. **22**(4): p. 195-207.
28. Bartok, O., et al., *Anti-tumour immunity induces aberrant peptide presentation in melanoma.* Nature, 2021. **590**(7845): p. 332-337.
29. Zhang, Z., et al., *Uniform genomic data analysis in the NCI Genomic Data Commons.* Nature Communications, 2021. **12**(1): p. 1226.
30. Verfaillie, A., et al., *Decoding the regulatory landscape of melanoma reveals TEADS as regulators of the invasive cell state.* Nat Commun, 2015. **6**: p. 6683.
31. Marin-Bejar, O., et al., *Evolutionary predictability of genetic versus nongenetic resistance to anticancer drugs in melanoma.* Cancer Cell, 2021. **39**(8): p. 1135-1149.e8.
32. Pozniak, J., et al., *A TCF4/BRD4-dependent regulatory network confers cross-resistance to targeted and immune checkpoint therapy in melanoma.* bioRxiv, 2022: p. 2022.08.11.502598.
33. Hugo, W., et al., *Genomic and Transcriptomic Features of Response to Anti-PD-1 Therapy in Metastatic Melanoma.* Cell, 2016. **165**(1): p. 35-44.
34. Oh, D.Y. and L. Fong, *Cytotoxic CD4(+) T cells in cancer: Expanding the immune effector toolbox.* Immunity, 2021. **54**(12): p. 2701-2711.
35. Shan, J., et al., *The C/ebp-Atf response element (CARE) location reveals two distinct Atf4-dependent, elongation-mediated mechanisms for transcriptional induction of aminoacyl-tRNA synthetase genes in response to amino acid limitation.* Nucleic Acids Res, 2016. **44**(20): p. 9719-9732.
36. Xiao, H., et al., *Precision glycocalyx editing as a strategy for cancer immunotherapy.* Proc Natl Acad Sci U S A, 2016. **113**(37): p. 10304-9.
37. Li, H., et al., *A male germ-cell-specific ribosome controls male fertility.* Nature, 2022.
38. Laumont, C.M., et al., *Noncoding regions are the main source of targetable tumor-specific antigens.* Sci Transl Med, 2018. **10**(470).
39. Ghasempour, S. and S.A. Freeman, *The glycocalyx and immune evasion in cancer.* The FEBS Journal, 2021. **n/a**(n/a).
40. Buffone, A., Jr. and V.M. Weaver, *Don't sugarcoat it: How glycocalyx composition influences cancer progression.* Journal of Cell Biology, 2019. **219**(1): p. e201910070.
41. Ponting, C.P. and W. Haerty, *Genome-Wide Analysis of Human Long Noncoding RNAs: A Provocative Review.* Annu Rev Genomics Hum Genet, 2022. **23**: p. 153-172.

42. Adrienne Vancura , A.H.G., Thorben Hennig , Carlos Pulido-Quetglas , Frank Slack , View ORCID Profile Rory Johnson , Simon Häfliger, *Is evolutionary conservation a useful predictor for cancer long noncoding RNAs? Insights from the Cancer lncRNA Census 3*.
43. Adnane, S., A. Marino, and E. Leucci, *LncRNAs in human cancers: signal from noise.* Trends Cell Biol, 2022.
44. Barrett, T., et al., *NCBI GEO: mining millions of expression profiles--database and tools.* Nucleic Acids Res, 2005. **33**(Database issue): p. D562-6.
45. Blankenberg, D., et al., *Galaxy: a web-based genome analysis tool for experimentalists.* Curr Protoc Mol Biol, 2010. **Chapter 19**: p. Unit 19.10.1-21.
46. Bolger, A.M., M. Lohse, and B. Usadel, *Trimmomatic: a flexible trimmer for Illumina sequence data.* Bioinformatics, 2014. **30**(15): p. 2114-20.
47. Howe, K.L., et al., *Ensembl 2021.* Nucleic Acids Res, 2021. **49**(D1): p. D884-d891.
48. Bray, N.L., et al., *Near-optimal probabilistic RNA-seq quantification.* Nature Biotechnology, 2016. **34**(5): p. 525-527.
49. Pimentel, H., et al., *Differential analysis of RNA-seq incorporating quantification uncertainty.* Nat Methods, 2017. **14**(7): p. 687-690.
50. Subramanian, A., et al., *Gene set enrichment analysis: a knowledge-based approach for interpreting genome-wide expression profiles.* Proc Natl Acad Sci U S A, 2005. **102**(43): p. 15545-50.
51. Wickham, H., *ggplot2: Elegant Graphics for Data Analysis*. 2016 Springer-Verlag New York.
52. Frankish, A., et al., *GENCODE reference annotation for the human and mouse genomes.* Nucleic Acids Res, 2019. **47**(D1): p. D766-d773.
53. Yates, A.D., et al., *Ensembl 2020.* Nucleic Acids Research, 2020. **48**(D1): p. D682-D688.
54. Marçais, G. and C. Kingsford, *A fast, lock-free approach for efficient parallel counting of occurrences of k-mers.* Bioinformatics, 2011. **27**(6): p. 764-770.
55. Gans, J.D. and M. Wolinsky, *Improved assay-dependent searching of nucleic acid sequence databases.* Nucleic Acids Research, 2008. **36**(12): p. e74-e74.
56. Rodriguez, J.M., et al., *APPRIS: annotation of principal and alternative splice isoforms.* Nucleic Acids Res, 2013. **41**(Database issue): p. D110-7.
57. Karras, P., et al., *A cellular hierarchy in melanoma uncouples growth and metastasis.* Nature, 2022. **610**(7930): p. 190-198.
58. Stringer, C., et al., *Cellpose: a generalist algorithm for cellular segmentation.* Nat Methods, 2021. **18**(1): p. 100-106.
59. Perico, L., et al., *Human mesenchymal stromal cells transplanted into mice stimulate renal tubular cells and enhance mitochondrial function.* Nature Communications, 2017. **8**(1): p. 983.
60. Ghandi, M., et al., *Next-generation characterization of the Cancer Cell Line Encyclopedia.*
61. Yang, W., et al., *Genomics of Drug Sensitivity in Cancer (GDSC): a resource for therapeutic biomarker discovery in cancer cells.* Nucleic Acids Res, 2013. **41**(Database issue): p. D955-61.
62. Kang, Y.J., et al., *CPC2: a fast and accurate coding potential calculator based on sequence intrinsic features.* Nucleic Acids Res, 2017. **45**(W1): p. W12-w16.

63. Ernlund, A.W., R.J. Schneider, and K.V. Ruggles, *RIVET: comprehensive graphic user interface for analysis and exploration of genome-wide translatomics data.* BMC Genomics, 2018. **19**(1): p. 809.

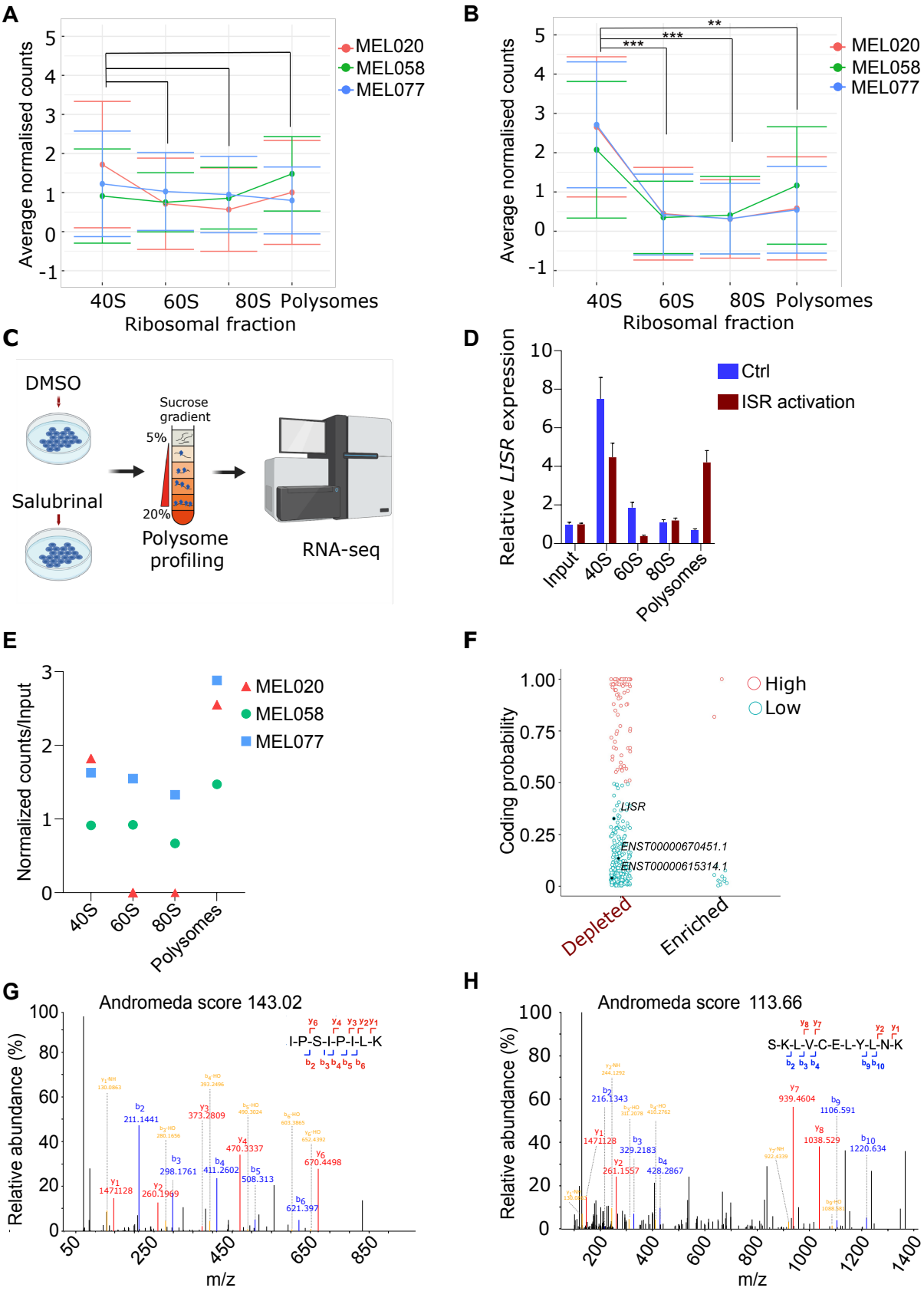

Figure 1: LISR is a lncRNA associated with polysomes during the ISR.

Figure 1: *LISR* is a lncRNA associated with polysomes during the ISR. A. Average mRNA counts per ribosomal fraction normalized to the average counts of the combined fractions per melanoma model. Significance was calculated by Tukey's multiple comparisons test. **B**. Average lncRNA counts per ribosomal fraction normalized on the average counts of the combined fractions per melanoma model. Significance was calculated by Tukey's multiple comparisons test.**C.**Experimental workflow: melanoma cells were treated with salubrinal to activate the ISR and extracts processed by polysome profile and RNA-Seq. **D.** RT- qPCR showing *LISR* expression in different ribosomal fractions. **E.** *LISR* counts per ribosomal fraction normalized to *LISR* counts of input samples in different melanoma PDX models. **F.** Coding probability (as determined by CPC2) of lncRNAs significantly and differentially expressed (threshold is FDR<0.05 and 0.5>FC>2 between salubrinal and control treated SKMEL28 cells. A score below 0.5 is expected for typical non- coding RNAs. **G.** Higher energy collisional dissociation (HCD) spectrum and full annotation of the doubly charged parent ion with m/z = 440.7983 (ENST00000615314.1 - IPSIPILK) in SK-MEL-28 before treatment with salubrinal. Andromeda score is reported as calculated by MaxQuant. Matched fragments are indicated in color (blue for b-ions, red for y-ions and yellow either for ammonia or water losses) **H.** Higher energy collisional dissociation (HCD) spectrum and full annotation of the doubly charged parent ion with m/z = 683.8756 (ENST00000670451.1 - SKLVCELYLNK) in SK-MEL-28 before treatment with salubrinal. Andromeda score is reported as calculated by MaxQuant. Matched fragments are indicated in color (blue for b ions, red for y ions and yellow either for ammonia or water losses).

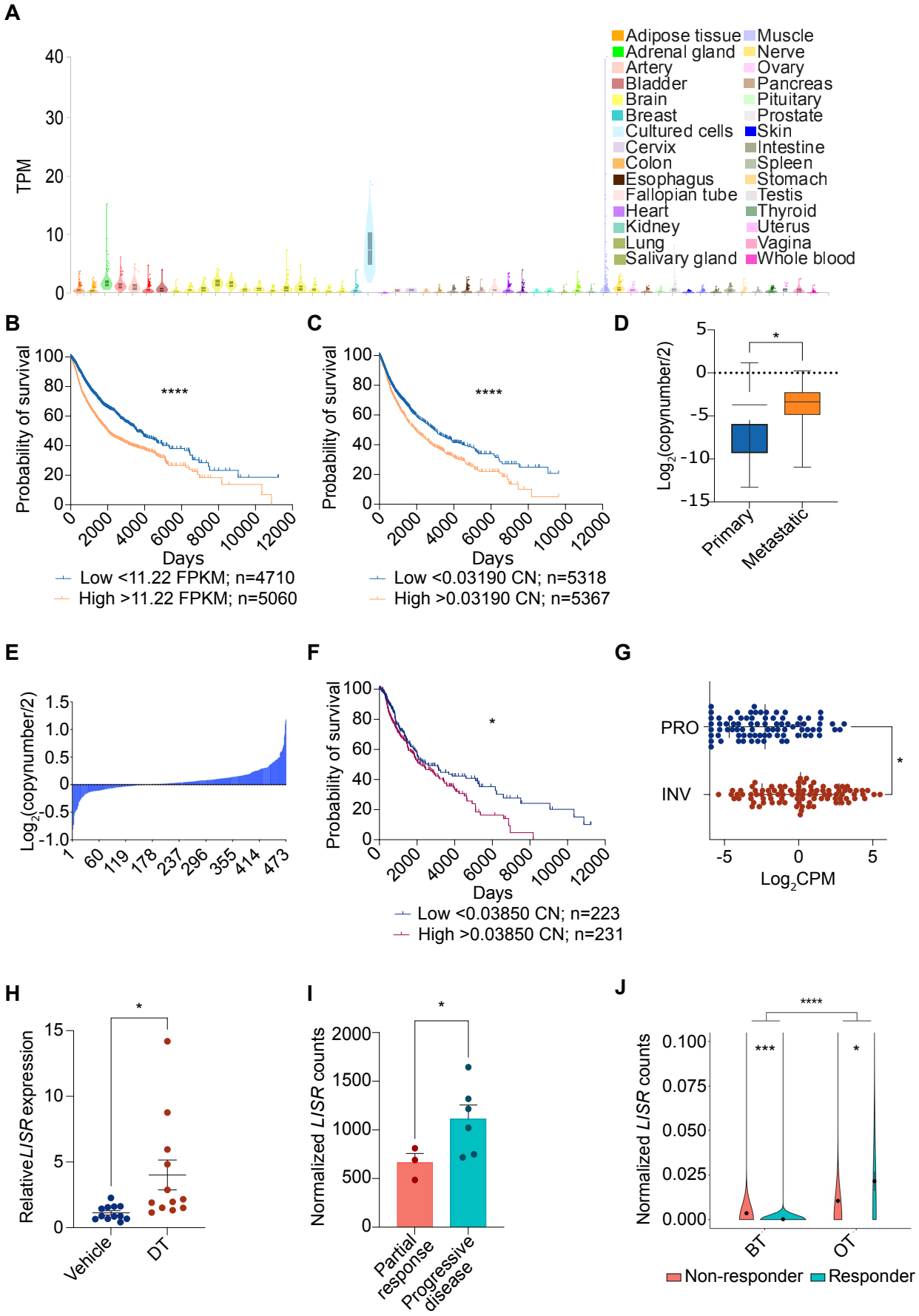

Figure 2A-J: LISR expression and copy number correlate with patient survival and responses to ICB

Figure 2A-J: *LISR* expression and copy number correlate with patient survival and responses to ICB. A. LISR expression in a panel of adult normal samples from the GTEX database. **B.** Overall survival of patients in the TGCA GDC Pan-Cancer cohort as a function of LISR expression Log-rank (Mantel-Cox) test was performed to calculate statistical significance. **C.** Overall survival of patients in the TGCA GDC Pan-Cancer cohort as a function of LISR DNA copy number expressed as Fragments Per Kilobase of transcript per Million reads (FPKM). Log-rank (Mantel-Cox) test was performed to calculate statistical significance. **D.** LISR DNA copy number in primary and metastatic samples from TCGA GDC Melanoma dataset. Unpaired t test was performed to calculate statistical significance. **E.** LISR DNA copy number amplification in melanoma samples from the TCGA GDC Melanoma dataset. **F.** Overall survival of patients in TCGA GDC Melanoma cohort as a function of LISR DNA copy number. Log-rank (Mantel-Cox) test was performed to calculate statistical significance. **G.** LISR expression in counts per million (CMP) in TGCA GDC Melanoma dataset with proliferative or invasive signature [30]. Unpaired t test was performed to calculate statistical significance. **H.** Measurement of LISR expression by RT-qPCR in a cohort of melanoma PDX models at relapse after treatment with a vehicle or with targeted therapy (DT). Unpaired t test was performed to calculate statistical significance. **I.** Expression of LISR (read counts normalized by Sleuth) in bulk RNA sequencing libraries derived from BRAF mutant patients partially or not responding to pembrolizumab. Each dot represents aggregate normalized counts of a single patient. [33]. Significance was calculated by likelihood ratio test. **J.** LISR expression (read counts normalized by Sleuth) in a melanoma cohort of responders and not responders to immune checkpoint blockade [32], before treatment (BT) and on treatment (OT). Significance was calculated by Mann Whitney test.

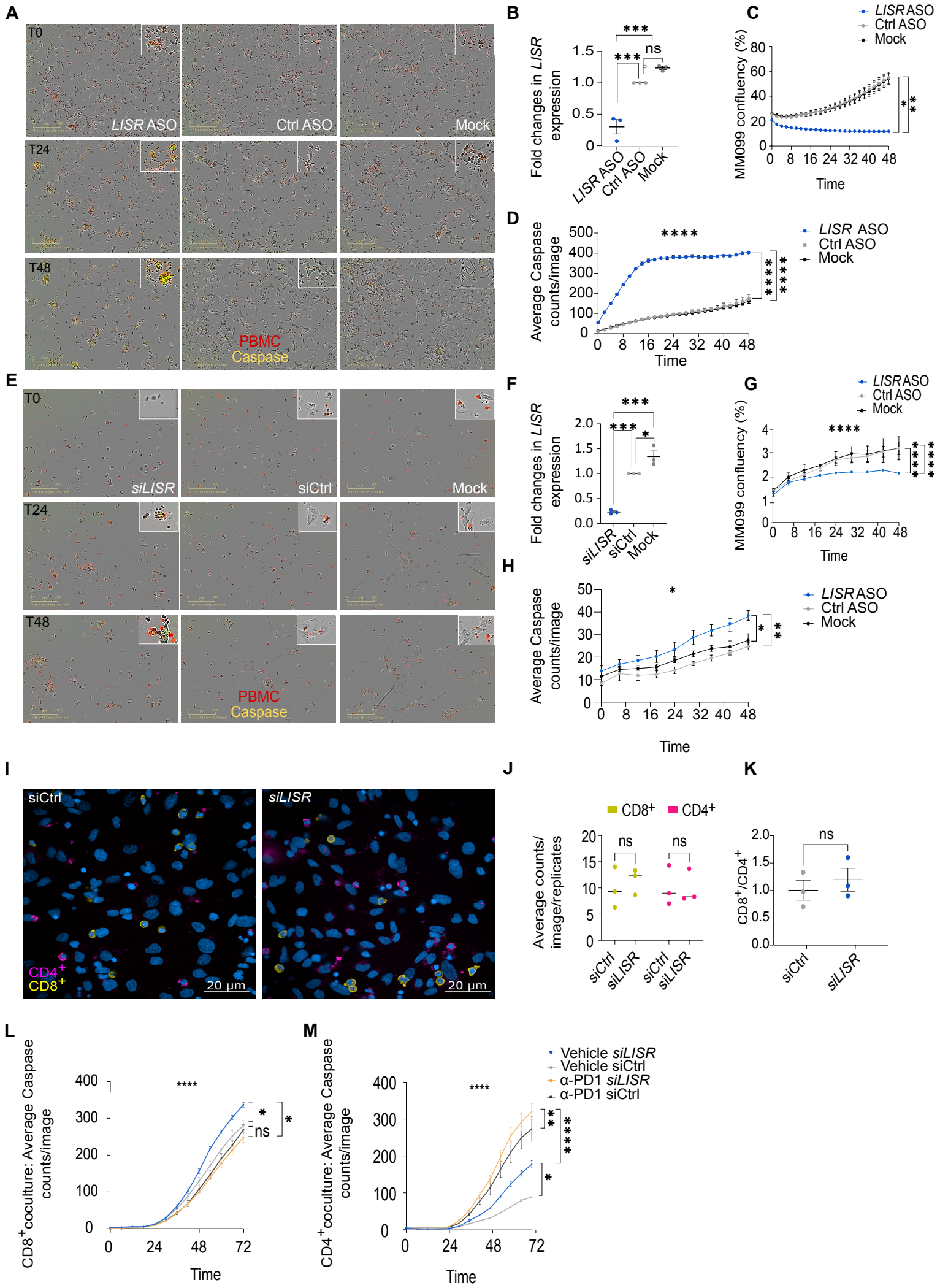

Figure 3A-M: Inhibition of LISR enhances anti-melanoma immune responses

Figure 3A-M: Inhibition of *LISR* enhances anti-melanoma immune responses. A. Representative pictures of PBMCs (RED) cocultured with MM099 melanoma cell line upon *LISR* KD using ASOs. Caspase-3$^+$ cells are in GREEN/YELLOW. **B.** Efficiency of *LISR* KD calculated by RT-qPCR and expressed as fold changes (FC) compared to Ctrl ASO. Statistics calculated by One-way ANOVA. **C.** Analysis of MM099 confluency (%) transfected with *LISR* ASO, ASO control (Ctrl ASO) or not transfected (MOCK) and co-cultured with PBMCs stimulated with IL-2 only. Statistics calculated Two-way ANOVA mixed effect. **D.** Analysis of Caspase-3 counts in MM099 transfected as indicated in A and cocultured with PBMCs stimulated with IL-2 only. Statistics were calculated by Two-way ANOVA mixed effect. **E.** Representative pictures of MM099 transfected with siRNAs against LISR (si*LISR*), non-targeting control (siControl) or not transfected (MOCK) and co-cultured with PBMCs (in RED) stimulated with a T-cell activating cocktail. Caspase-3$^+$ cells are in GREEN/YELLOW. **F**. Efficiency of *LISR* KD in experiment in E, calculated by RT-qPCR and expressed as FC compared to Ctrl ASO. **G**. MM099 confluency in the experiment in E. Statistics calculated by Two-way ANOVA mixed effect**. H.** Caspase counts in the experiment in E. Statistics were calculated by Two-way ANOVA mixed effect. **I.** Confocal images of MM099 and PBMCs cocultures in E. In blue nuclei, CD4+ and CD8+ cells are in magenta and in yellow respectively. **J.** Quantification of confocal images from the experiment in I. Average counts of CD4+ and CD8+ per images per biological replicate are shown. Statistics calculated by Two-Way ANOVA. **K.** Ratio CD8+/CD4+ cells from experiment in I. **L.** Caspase counts in coculture of CD8+ cells with MM099 transfected transfected as indicated in E and treated with α-PD1. Statistics calculated by Two-way ANOVA mixed effect analysis. **M.** Caspase counts in coculture of CD4+ cells with MM099 transfected as indicated in E and treated with α-PD1. Statistics calculated by Two-way ANOVA mixed effect analysis.

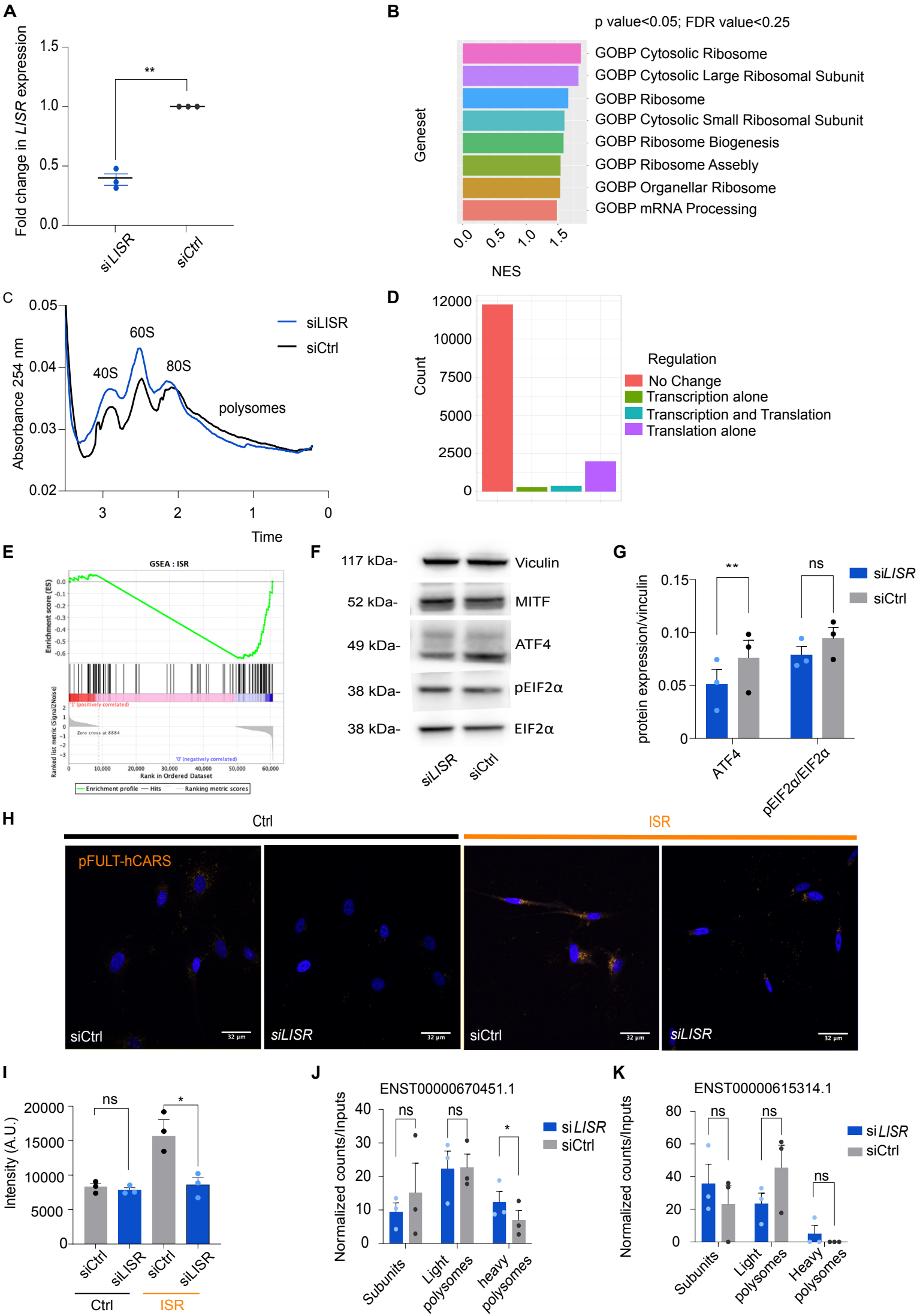

Figure 4A-K: LISR regulates translation

Figure 4A-K: *LISR* regulates translation. A. Efficiency of *LISR* KD as calculated by RT-qPCR. Values are expressed as Fold changes. Paired t test was performed to calculate statistical significance. **B.** GSEA on bulk RNA sequencing data from MM099 cells upon *LISR* KD. Threshold values p-value<0.05; FDR-val<0.25; NES>0. **C.** Polysome profiling diagram upon *LISR* KD. **D.** Effect of LISR KD on the transcriptome and translatome as calculated by Ribosomal Investigation and Visualization to Evaluate Translation (RIVET) [63] analysis on bulk RNA sequencing data from polysome profiling of MM099 cells upon *LISR* KD. **E.** Correlation between bulk RNA sequencing data from ribosome profiling of MM099 cells upon *LISR* KD and the ISR translational signature by GSEA (nominal p-value = 0.02259887). **F.** Western blot for MITF, ATF4, peIF2α and eIF2 α upon *LISR* KD. Vinculin was used as loading control. **G.** Densitometric analysis of the western blot in F. Paired t test was performed. **H.** Confocal images showing cells infected with pFULThCARS reporter in control condition (DMSO) and upon ISR induction (salubrinal). Nuclei are in BLUE and pFULThCARS is in ORANGE. **I.** Quantification of fluorescence of pFULT-hCARS reporter in Mel-015 cells upon *LISR* KD and ISR activation. **J.** ENST00000670451.1 enrichment at different ribosomal fractions (normalized counts on input) as determined by bulk RNA sequencing on ribosome profiling fractions. Significance was calculated byRIVET analysis. **K**. ENST00000615314.1 enrichment at different ribosomal fractions (normalized counts on input) as determined by bulk RNA sequencing on ribosome profiling fractions. Significance was calculated by RIVET analysis.

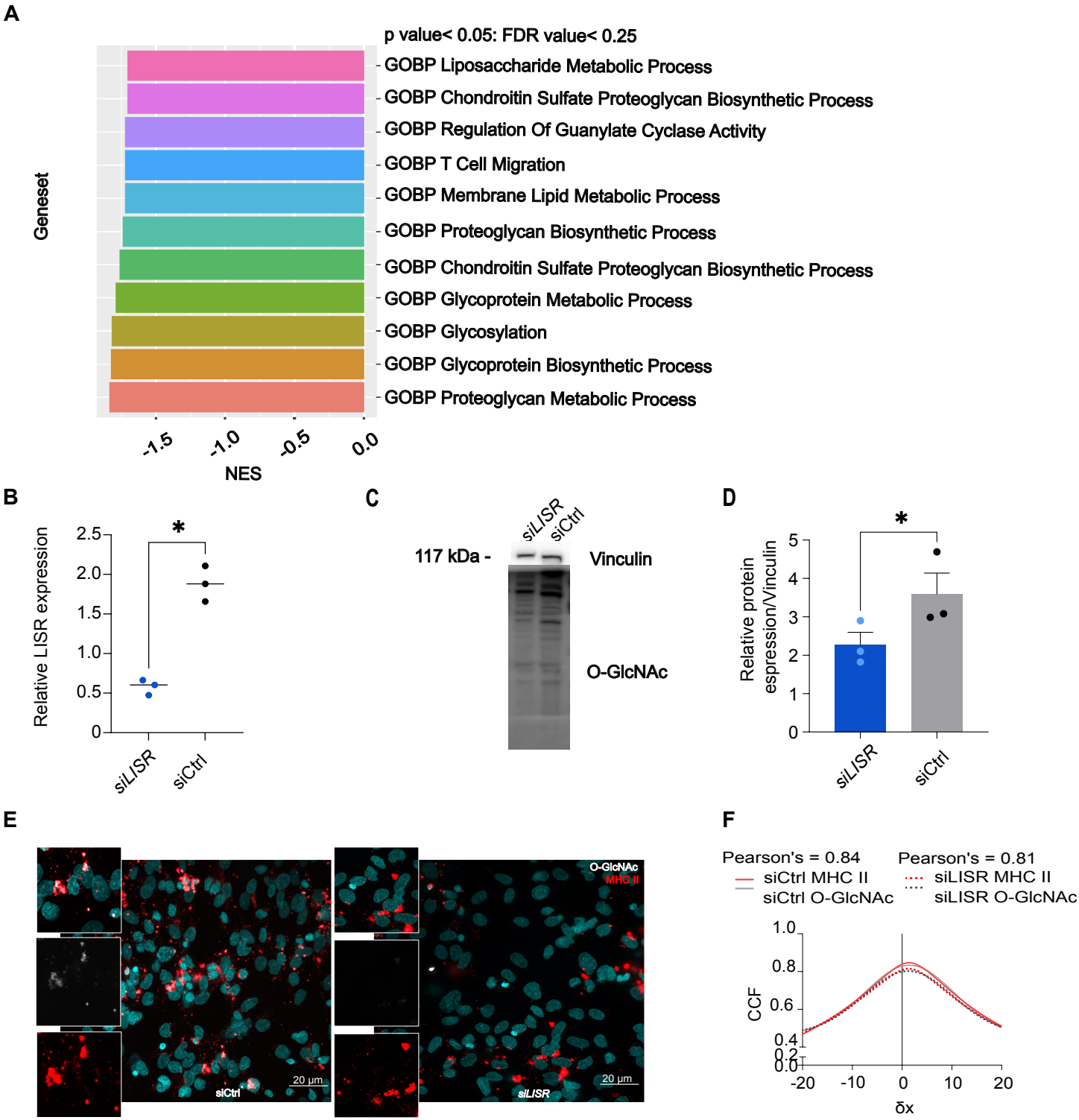

Figure 5A-F: LISR enhances glycosylation

Figure 5A-F: *LISR* enhances glycosylation. A. GSEA on bulk RNA sequencing data from ribosome profiling of MM099 cells upon *LISR* KD. Threshold values p-value<0.05; FDR-val<0.25; NES>0. **B.** Efficiency in *LISR* KD as calculated by RT-qPCR and expressed as FCcompared to the Ctrl ASO.**C.** Western Blot for O-linked N-acetylglucosamine in MM099 upon *LISR* KD. Vinculin was used as a loading control. **D.** quantification of the graph in C. **E.** Immunostaining for MHCII and O-linked N-acetylglucosamine (gray) in melanoma cell (RED). **F.** Evaluation of the level of colocalization as measured by Cross correlation function (CCF) with a pixel shift of δ = ±20.

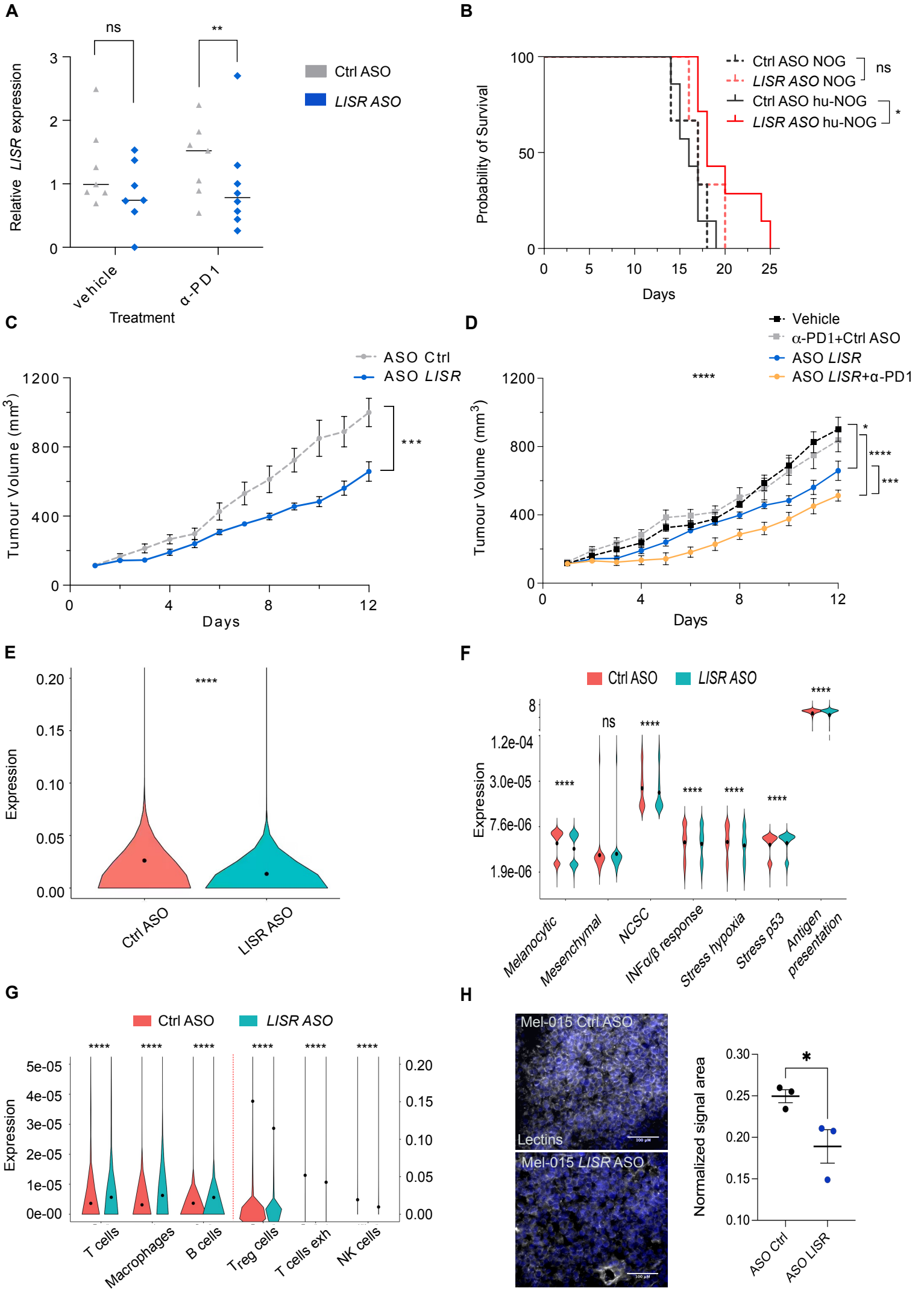

Figure 6A-H: Inhibition of LISR overcomes primary resistance to ICB.

Figure 6A-H: Inhibition of *LISR* overcomes primary resistance to ICB. A. Efficiency of LISR KD *in vivo* in PDX models upon systemic administration of an ASO against *LISR* or a non-targeting control. Multiple t test was performed to calculate statistical significance. **B**. Kaplan-Meier plot of immune deficient and immunocompetent mice upon systemic inhibition of *LISR*. **C.** Comparison of the tumor growth over time of humanized PDX melanoma models treated with an antisense against *LISR* (*LISR* ASO n=7), a non-targeting control (Ctrl ASO n=7) or a vehicle (n=5). Two-way ANOVA mixed effect was performed to calculate statistical significance. **D.** Comparison of the tumor growth over time of humanized PDX melanoma models treated with an antisense against *LISR* (*LISR* ASO n=7), with α- PD1 (n=6), or with a combination of the two (ASO+α-PD1 n=5). Two-way ANOVA mixed effect was performed to calculate statistical significance. **E.** Quantification at single cell resolution, of *LISR* KD in hu-PDX tumour sections described in C as calculated by smFISH. **F.** Effect of *LISR* KD on the expression of drug-tolerant melanoma signatures as assessed by smFISH and molecular cartography. **G.** Effect of *LISR* KD on the expression of immune cell markers and exhaustion markers as assessed by smFISH and molecular cartography. **H.** Staining for lectins in hu-PDX tumour sections described in C and its quantification. Nuclei are labelled with DAPI in BLUE. Lectins are in gray. P value was calculated by unpaired t-test.